Manuscript prepared for The Cryosphere
with version 2014/09/16 7.15 Copernicus papers of the LaTeX class copernicus.cls.
Date: 30 November 2017

Accumulation patterns around Dome C, East Antarctica, in the last 73 kyrs

Marie G.P. Cavitte[1,2], Frédéric Parrenin[3], Catherine Ritz[3], Duncan A. Young[1], Brice Van Liefferinge[4], Donald D. Blankenship[1,2], Massimo Frezzotti[5], and Jason. L. Roberts[6,7]

[1]Institute for Geophysics, Jackson School of Geosciences, University of Texas at Austin, Austin, Texas, USA
[2]Department of Geological Sciences, Jackson School of Geosciences, University of Texas at Austin, Austin, Texas, USA
[3]Univ. Grenoble Alpes, CNRS, IRD, IGE, F-38000 Grenoble, France
[4]Laboratoire de Glaciologie, Université libre de Bruxelles, CP 160/03, Avenue F.D. Roosevelt 50, B-1050 Brussels, Belgium
[5]ENEA, Agenzia Nazionale per le nuove tecnologie, l'energia e lo sviluppo sostenibile, Rome, Italy
[6]Australian Antarctic Division, Kingston, Tasmania 7050, Australia
[7]Antarctic Climate & Ecosystems Cooperative Research Centre, University of Tasmania, Hobart, Tasmania 7001, Australia

Correspondence to: Marie G.P. Cavitte (mariecavitte@gmail.com)

Abstract. We reconstruct the pattern of surface accumulation in the region around Dome C, East Antarctica, since the last glacial. We use a set of 18 isochrones spanning all observable depths of the ice column interpreted from various ice-penetrating radar surveys and a 1D pseudo-steady ice flow model to invert for time-averaged accumulation rates in the region. The shallowest four isochrones are then used to calculate paleoaccumulation rates between isochrone pairs using a 1D assumption where horizontal advection is negligible in the time interval of each layer. We observe that the large-scale (100s km) surface accumulation gradient is spatially stable through the last 73 kyrs, which reflects current modeled and observed precipitation gradients in the region. We also observe small-scale (10s km) accumulation variations linked to snow redistribution at the surface due to changes in its slope and curvature in the prevailing wind direction that remain spatially stationary since the last glacial.

1 Introduction

The Dome C region, located on the East Antarctic interior plateau, has long been the focus of extensive research: it is the site of the oldest as-yet-retrieved continuous ice core, the EPICA Dome C ice core, going back ~800 ka (Parrenin et al., 2007). Modern surface precipitation on the Dome C plateau is extremely low (~25 mm yr^{-1}, Stenni et al., 2016), with infrequent storm events representing more than 50% of the total annual precipitation (Frezzotti et al., 2005). Coastal air masses lose moisture as they are driven inland to higher elevation, resulting in a characteristic precipitation gradient with higher measured and modeled precipitation on the north side of Dome C (Arthern et al., 2006; Genthon et al., 2016; Kållberg et al., 2004; Gallée et al., 2013; Palerme et al., 2014; Van Wessem et al., 2014). Present-day moisture-bearing air mass trajectories (Scarchilli et al., 2011; Genthon et al., 2016) point to a western Indian Ocean provenance for the snow precipitation at Dome C (85% of the precipitation), and suggest this could have persisted through glacial-interglacial cycles.

Snow precipitation is homogeneous at a large-scale, whereas local variations in snow accumulation are controlled by local surface topography as a function of wind direction. Black and Budd (1964) and Budd (1971) are the first to observe the close relationship between bedrock relief, surface slope and accumulation rates in Wilkes Land. Whillans (1975) details how wind speed and direction can affect total mass balance in Marie Byrd Land. Frezzotti et al. (2007) show that surface slope in the prevailing wind direction (SPWD) is a key constraint in determining spatial and temporal variability of precipitation; a higher SPWD can lead to significant ablation and redeposition of snow (Frezzotti et al., 2002b, a, 2005, 2007). Das et al. (2013) show that SPWD is a strong threshold for the formation of wind scour or megadune fields. Evidence for a persistent westerly wind circulation pattern comes from mineral dust measured at EPICA Dome C which shows a uniform geographic provenance from South America and Australia to the East Antarctic plateau during glacial-interglacial cycles (Delmonte et al., 2010; Albani et al., 2012).

Airborne and ground-based ice-penetrating radar data have long been used to constrain the surface and bedrock topography over large parts of the Antarctic Ice Sheet (Gudmandsen, 1971; Drewry et al., 1980; Millar, 1981; Siegert, 2003; Bingham and Siegert, 2009, and many others), as well its internal stratigraphy (e.g. Siegert, 1999; MacGregor et al., 2012; Cavitte et al., 2016). Because the internal stratigraphy represents isochronal surfaces throughout much of the ice sheet, dated internal radar reflectors can be used to directly constrain the surface mass balance of the ice sheet in the highest part of the ice column (Medley et al., 2013; Verfaillie et al., 2012). Reconstructing accumulation history from deeper isochrones is more ill-posed as both accumulation variations and changes in ice flow can affect isochrone geometries (e.g. Koutnik et al., 2016; Neumann et al., 2008; Parrenin and Hindmarsh, 2007; Parrenin et al., 2006; Waddington et al., 2007; Nereson and Waddington, 2002), and assumptions have to be made about one or the other (Martin et al., 2009; Leysinger Vieli et al., 2011; Siegert, 2003; Morse et al., 1998, see companion paper for more discussion). Assumptions on the vertical strain rate will also affect reconstructed paleoaccumulation rates (e.g. MacGregor et al., 2015; Waddington et al., 2007, etc.). Several radar isochrone studies have shown the existence of a coast-to-dome precipitation gradient: Verfaillie et al. (2012) show a continuous existence of a precipitation gradient through the last 300 years, while Siegert (2003) shows the persistence of a strong accumulation gradient between Dome C and Ridge B (a topographic high upstream of Lake Vostok) over glacial-interglacial timescales.

Better constraining accumulation rates through time is important for several reasons:

1. The spatial distribution of snow accumulation affects the position of topographic domes, which ultimately affects the geometry of the ice sheet (with its resulting sea-level implications) through time (Scarchilli et al., 2011; Fujita et al., 2011; Morse et al., 1998).

2. In addition to other parameters, accumulation rates are required for accurate dating and interpretation of ice cores. Constraints on accumulation and flowline geometries of ice particles through time are necessary to reconstruct ice core chronologies and correct for the effects associated with deposition at a different location and elevation than the ice coring site (Koutnik et al., 2016; Parrenin et al., 2007). Especially in the context of the search for 1.5 million-year-old ice, such constraints will have a significant influence on the choice of an ice core site.

3. The temporal evolution of accumulation rates provides important constraints on ice sheet mass balance through time for modeling experiments (Koutnik et al., 2016; Fischer et al., 2013).

Here, we reconstruct paleoaccumulation rates for the Dome C region using a 1D pseudo-steady ice flow model (described in the companion paper: Parrenin et al., 2017) for the last 73 kyrs using the isochronal constraints obtained from radar surveys. We discuss the large-scale accumulation and small-scale variations in accumulation calculated around Dome C. We do not attempt to reconstruct paleoaccumulation further back in time due to the 1D assumptions and the increasing horizontal advection with depth.

2 Methods

2.1 Dome C region

The Dome C region represents a topographic high in the middle of the EAIS and is at the confluence of several ice divides, the largest of which separates the Byrd Glacier catchment from the Totten Glacier catchment. The topography of the Dome C region is gentle: the change in elevation is ~10 m across 50 km (Genthon et al., 2016), reaching a maximum elevation at Dome C of ~3266 m above sea level (geoid height). A saddle connects Dome C to Lake Vostok along the ice divide, with a secondary dome referred to as “Little Dome C” (LDC) just south of the Dome C ice core site. The bedrock is characterized by a large subglacial massif ~40 km to the south of the Dome C ice core site and ~10 km south of the LDC, easily identifiable on Fig.1, where the radar survey grid is tightest. For ease of description, we refer to it as the “Little Dome C Massif” (LDCM) to differentiate from the surface topographic high. The deep Concordia Subglacial Trench (CST) runs along its eastern edge and is followed by a steep ridge, ~2000 meters high (Young et al., 2017), which we will refer to as the Concordia Ridge (CR). Both the LCDM and the CR (see Fig.1) have been identified as promising targets for retrieving 1.5 million-year old ice (Van Liefferinge and Pattyn, 2013).

2.2 Radar data

We use several airborne ice-penetrating radar surveys collected in the Dome C region by the University of Texas at Austin Institute for Geophysics (UTIG) and the Australian Antarctic Division (AAD) as part of the ICECAP project (International Collaborative Exploration of the Cryosphere through Airborne Profiling, Cavitte et al., 2016) and the Oldest Ice candidate A (OIA) survey flown by ICECAP in January 2016 (Fig.1, Young et al., 2017). All surveys use the same center frequency of 60 MHz, and the same bandwidth of 15 MHz; radar isochrones can therefore be easily matched from one season to the next. A set of 18 isochrones are traced throughout the region, using multiple crossovers, thus ensuring the reliability of the tracing as outlined in Cavitte et al. (2016). The co-location of the EPICA Dome C ice core in the survey region enables the dating of the isochrones using the AICC2012 chronology (Bazin et al., 2013; Veres et al., 2013). Obtaining ages and associated uncertainties for each isochrone is described in Cavitte et al. (2016). We extend the same isochrones to the newly acquired OIA survey and add a number of shallower and deeper isochrones in the OIA region (Cavitte et al., in prep.). We use all 18 isochrones for the 1D model inversion but only use the youngest four isochrones going back into the last glacial (10 - 73 ka) for paleoaccumulation reconstructions, explained below. All four isochrone depths, ages and uncertainties at the Dome C ice core site are given in Table 1.

2.3 Modeling

We use 18 radar isochrones, dated from 10 ka (before 1950) to 366 ka, and the 1D pseudo-steady ice flow model described in the companion paper (Parrenin et al., 2017). The model inverts for time-averaged geothermal heat flux (G_0), time-averaged accumulation rate ($\bar{a}$), and time-averaged vertical strain rate profile parameter (p') every kilometer along a radar line. Pseudo-steady-state means that all parameters in the model are considered steady except for $R(t)$, a temporal factor applied to both basal melting and accumulation (see companion paper). In other words, we can split the accumulation rate into a time-averaged component $\bar{a}(x)$ that varies spatially, and a temporally varying component, $R(t)$:

$$a(x,t) = \bar{a}(x)R(t) \tag{1}$$

$\bar{a}(x)$ therefore is the time-averaged accumulation rate at a certain point x, while $R(t)$ represents the variations in accumulation rate over glacial-interglacial cycles over time. The model assumes that $R(t)$ is spatially invariant over the entire study region. $R(t)$ is obtained from AICC2012 inferred accumulation variations (Veres et al., 2013; Bazin et al., 2013), and represents the ratio of the accumulation at time t to the average accumulation over the last 800 kyrs.

When inverting the radar isochrones using the pseudo-steady ice flow model, ages and accumulations are all used in steady-state form, with glacial-interglacial accumulation variations normalized. The calculated time-averaged accumulation rate $\bar{a}$ (Fig.3), p', and G_0 result from the best fit of all the radar isochrone depths (dropping x for simpler notation). However, some differences between modeled and observed isochrones remain as all isochrones have to be simultaneously fitted for each point x. The 18 isochrones have to be used in the inversion as the deepest isochrones provide the strongest constraints on p' and G_0.

To reconstruct paleoaccumulation rates through time $\bar{a}_{\Delta\chi}$, where $\Delta\chi$ represents a discrete age interval, we use the G_0 and p' values calculated and assume they remain unchanged over each time so that the remaining misfit between modeled and observed isochrones is entirely a result of the uncertainty in $\bar{a}$. $\bar{a}_{\Delta\chi}$ represents the time-averaged paleoaccumulation rate for a layer with an age interval $\Delta\chi$, bounded above and below by a radar isochrone of AICC2012 age. We refer to these as isochrone-bounded layers. To calculate $\bar{a}_{\Delta\chi}$ values for each layer, we adjust the value of $\bar{a}$ such that modeled and observed isochrone-bounded layer age intervals $\Delta\chi$ are fitted perfectly for each layer.

In mathematical form, if z is the depth of the isochrone and χ the age of the isochrone, we can write the isochrone-bounded layer's age interval in steady-state form as:

$$\Delta\chi_m^{steady} = \int_{z_1}^{z_2} \frac{dz}{\tau(z)\bar{a}_{m,\Delta\chi}} \text{, for the model,} \tag{2}$$

and

$$\Delta\chi_o^{steady} = \int_{z_1}^{z_2} \frac{dz}{\tau(z)\bar{a}_{o,\Delta\chi}} \text{, for observations,} \tag{3}$$

where τ is the vertical thinning function, i.e. the ratio of the vertical thickness of a layer to its initial vertical thickness at the surface, and $\Delta\chi^{steady}$ is the steady-state age interval $\Delta\chi$ using Eq.1.

We want to obtain $\bar{a}_{o,\Delta\chi}$, the "observed" paleoaccumulation rate for a certain age interval $\Delta\chi$. This is similar to the "shallow-layer approximation" used by Waddington et al. (2007).

Assuming all errors arise from the accumulation rate uncertainty is equivalent to assuming τ is modeled perfectly. Therefore we can equate Eq.2 with Eq.3 and obtain $\bar{a}_{o,\Delta\chi}$:

$$\bar{a}_{o,\Delta\chi} = \frac{\Delta\chi_m^{steady}}{\Delta\chi_o^{steady}} \bar{a}_{m,\Delta\chi} \tag{4}$$

Using Eq.4, we calculate the best fit time-averaged paleoaccumulation rates through time in one iteration after the model inversion. The values of $\bar{a}_{o,\Delta\chi}$ obtained are the time-averaged paleoaccumulation for each isochrone-bounded layer of age interval $\Delta\chi$. This gives the spatial variations of the paleoaccumulation rates through time.

To respect our assumption that τ is modeled perfectly, we only calculate paleoaccumulation rates $\bar{a}_{o,\Delta\chi}$ for the first four isochrone-bounded layers. Our fourth and deepest layer used reaches an average depth of 30% of the ice thickness, with calculated thinning never reaching below 0.6. Furthermore, to avoid ill-posed conditions for our 1D paleoaccumulation reconstructions, we only retain data points that have experienced a maximum of 5 km of horizontal advection. We do this for each layer, using Van Liefferinge and Pattyn (2013) ice surface balance velocities, corrected for temporal velocity variations using $R(t)$ (Parrenin et al., 2017), and the age interval spanned by the layer considered. Any point that has traveled more than 5 km horizontally is masked.

Temporal variations $R(t)$ of the accumulation rates have been ignored until this point. We use Eq.1 and calculated $R(t)$ values from the AICC2012 chronology accumulation variations to obtain the corresponding paleoaccumulation rates, $a_{o,\Delta\chi}$. We show the paleoaccumulation rates calculated for the four youngest age intervals spanning 0 - 73 ka in Fig.2 and 4.

Care must be taken in not over-interpreting the paleoaccumulation maps obtained. We do not argue that we have reconstructed absolute paleoaccumulations for the past 73 kyrs. The 1D pseudo-steady ice flow model used here (see companion paper, Parrenin et al., 2017) does not take horizontal advection into account. Paleoaccumulation rates calculated are valid at the ice divide and the dome where horizontal ice flow speeds are negligible. Farther away, horizontal advection has a larger influence. A full 3D model is required to reconstruct accumulation rates more extensively in space and further in time.

The Metropolis-Hastings (MH) algorithm (described in the companion paper, Parrenin et al., 2017) enables the calculation of an accumulation rate uncertainty which takes into account the age uncertainty of the radar isochrones (see S2). The age uncertainty of the radar isochrones is a combination of the radar depth uncertainties translated to age uncertainties (Cavitte et al., 2016) and the AICC12 ice core chronology uncertainties (Veres et al., 2013; Bazin et al., 2013). Cavitte et al. (2016) describe the various sources of radar depth uncertainty and how they are calculated. The radar isochrone depth and age uncertainties are given in Table 1. We plot the time-averaged accumulation rate and the paleoaccumulation rates for each isochrone-bounded layer over the survey region (see Fig.3, 4). The accumulation rate uncertainties are given in Fig. S2 and further discussed in Supplement 2.

2.4 ECMWF ERA40 snow precipitation rate

The snow accumulation rates in the Dome C region result from precipitation in the form of snow (snowfall and diamond dust), then modified by wind-driven processes. The wind erosion, wind redistribution and sublimation, as well as other processes during or after a precipitation event, leads to spatial deposition at the surface that is much less homogeneous than the original precipitation (e.g., Frezzotti et al., 2004). To compare large-scale patterns of precipitation to independent measurements, ECMWF (European Center for Medium-Range Weather Forecasts) ERA40 re-analysis data (Simmons et al., 2007) is used to obtain a map of present-day estimated precipitation rates over the survey region. The ECMWF ERA40 model seems to correctly reproduce the observed precipitation's spatial and temporal variability at Dome C, but systematically underestimates the precipitation magnitudes (Genthon et al., 2016; Stenni et al., 2016), probably because clear-sky precipitation is not adequately parameterized (Bromwich et al., 2004; Van de Berg et al., 2006). The ECMWF ERA40 model does not reproduce snow accumulation because it does not consider the blowing snow transport/sublimation process. However, since the Dome C site is not influenced by strong winds, this is expected to have a minor effect within the summit area, but cannot be completely neglected farther than 25 km from the dome/ice divide. ECMWF ERA40 data have been normalized using the surface accumulation average of the last centuries from existing ground-penetrating radar (GPR) within 25 km from Dome C summit (Urbini et al., 2008).

A number of steps went into adjusting the ECMWF ERA40 modeled precipitation rates to field measurements, to calculate the "ECMWF ERA40 estimated present-day surface accumulation rates", shown in Fig.5. These steps are:

1. ECMWF ERA40 monthly average precipitation rates were used to calculate a long term precipitation average over the 1989 - 2011 period
2. Precipitations were then interpolated over the region of interest as a 1 km grid
3. Precipitation values were increased by 12.9 mm yr^{-1} to match GPR measurements in the area (Urbini et al., 2008) as ECMWF ERA40 precipitation values are systematically too low compared to ground-based measurements.

Independent traverse accumulation measurements confirm the calculated accumulations (Emmanuel Le Meur, pers comm.)

2.5 Detrending paleoaccumulation rates

To look at small-scale paleoaccumulation variations more closely, we remove large-scale precipitation gradients (see Sect.4). For this, we calculate a quadratic fit of the ECMWF ERA40 present-day surface accumulation values (calculated as described above) with each isochrone-bounded layer's paleoaccumulation, and subtract the calculated fit from the layer's paleoaccumulation values. The result is a map of detrended paleoaccumulations for each isochrone-bounded layer (Fig.6).

2.6 Slope and Curvature in the Prevailing Wind Direction (SPWD and CPWD)

In Sect.4, we discuss the importance of surface slope in the prevailing wind direction (SPWD) and curvature in the prevailing wind direction (CPWD). We use ECMWF 5-year average wind directions (Simmons et al., 2007) and Bamber et al. (2009) surface elevations to calculate SPWD and CPWD values over a 3 km radius in the survey region (Fig.6). A positive value of surface curvature indicates a surface trough, while a negative value of surface curvature indicates a surface bump.

3 Results

We use a standard MH algorithm to run the pseudo-steady ice flow model to invert for time-averaged $\bar{a}$, p' and G_0. Values of the time-averaged $\bar{a}$, p' and G_0 and their uncertainties are obtained after

1000 MH iterations, each taking 5 thermo-mechanical iterations (see companion paper, Parrenin et al., 2017). Parrenin et al. (2017) describe the results obtained and the parameter priors used for the inversion. Here, we focus on the accumulation rate reconstructions $\bar{a}$, and $a_{o,\Delta\chi}$ obtained using Eq.4.

The reconstructed paleoaccumulations $a_{o,\Delta\chi}$ are shown in the top panel of Fig.2 along the A-A' radar transect (VCD/JKB2g/DVD01a) marked on Fig.1. Ages given are the mean of the age interval represented in each paleoaccumulation rate. The A-A' radar line runs along the ice divide, and a marked decreasing accumulation rate can be seen going from the northeast side towards the southwest consistently over all age intervals. Bottom panel of Figure 2 displays $a_{o,\Delta\chi}$ along the B-B' radar transect (OIA/JKB2n/Y77a) marked on Fig.1. This transect runs across the divide and there is no clearly visible spatial accumulation gradient for all age intervals, except a weaker one for the interglacial 10 ka isochrone. This is expected as the southern end of this radar line is on the high-accumulation side of the divide.

We also show reconstructed accumulation rates in map view in Fig.3 and 4. Fig.3 displays the time-averaged accumulation rate $\bar{a}$ and Fig.4 displays the paleoaccumulation rate per isochrone-bounded layer $a_{o,\Delta\chi}$. We show all four age intervals calculated. We observe that the time-averaged accumulation (Fig.3) has a clear north to south gradient, decreasing from $>$ 21 mm water equivalent per year (mm-we yr^{-1}) in the north to 15 mm-we yr^{-1} in the south. Superimposed, we observe a number of regions ~20 km wide that show a ~25% accumulation increase over the LDCM, to ~50 km wide or more east of the CR with a ~75% increase. These are outlined by black lines on Fig.3. Around the CR, we also note that the extended area of high accumulation is adjacent to an area of very low accumulation, parallel to it and just east of the CST. This corresponds to an area of drastic surface slope and curvature change (see also Fig.6, S3, and S4).

The spatial pattern of paleoaccumulation rates per isochrone-bounded layer (Fig.4) is similar to that of the time-averaged accumulation: a large-scale gradient N-S with superimposed areas of higher accumulation in the same locations as for the time-averaged accumulation reconstruction. We note a striking similarity between the time-averaged accumulation rate (Fig.3) and the paleoaccumulation rates for the ages 0 ka - 10 ka (Fig.4). We also note that accumulation rates are higher for the interglacial age interval (0 ka - 10 ka) than for the glacial age intervals (see Fig.4 and S4). The small-scale accumulation patterns are visible in the 0 - 10 ka age interval, we see the same three areas of high accumulation as outlined in Fig.3. For older layers, the smaller spatial extent of the paleoaccumulation data makes it difficult to conclude on the persistence of these small-scale high accumulation areas.

Bedrock elevations from Bedmap2 (Fretwell et al., 2013) augmented with new OIA survey data outlined with a dashed rectangle (Young et al., 2017), as well as Bamber et al. (2009) surface elevation contours, are plotted in the background of Fig.3 and 4. The areas of higher accumulation are co-located with areas of low surface slopes, visible from the surface contours. The accumulation variations we observe are also co-located with significant bedrock relief changes, which reach e.g. ~2000 m for the CR escarpment, and ~500 m for the south side of the LDCM (see Fig. S1).

We use the time-averaged accumulation, $\bar{a}$, obtained from the model and Eq.1 to plot Holocene average accumulation rates. For this, we take the ratio of the average accumulation rate of the last 100 years to that of the last 800 kyrs using the AICC2012 chronology, which has a value of 0.65. The time-averaged $\bar{a}$ is scaled by this factor of 0.65 to obtain Holocene average accumulation rates, which we call a_{100yrs} here. We plot a_{100yrs} together with ECMWF ERA40-derived surface accumulation data in Fig.5 (see Sect.2.4 for details). We observe that the large-scale N-S accumulation gradient in a_{100yrs} closely resembles that of the ECMWF ERA40-derived surface accumulation rate in Fig.5: high accumulation in the north nearer the coast, and lower accumulation in the south as you move towards the interior. The magnitude of the accumulation rates also matches surprisingly well.

The calculated accumulation rate uncertainties from the model, with an average value of 0.16 mm-we yr^{-1} (see Fig. S2), are an order of magnitude (or more) smaller than the values of reconstructed time-averaged accumulation rate, providing confidence in the time-averaged accumulation rates calculated. However errors have been treated as uncorrelated so we cannot apply these uncertainties to the paleoaccumulations. We hope to improve this in the future.

To focus on the small-scale variations in paleoaccumulations, we plot detrended paleoaccumulations (see Sect.2.5) for the region on top of SPWD and CPWD values (see Sect.2.6), as shown on Fig.6. We only show this relationship for the first layer, spanning the past 10 kyrs, as older layers are not as extensive. Looking at the spatial distribution of these detrended paleoaccumulations in relation to SPWD, we observe that areas with high accumulation are co-located with areas of markedly reduced SPWD values with respect to the surrounding values (~0.5-1.2 x 10^{-3} of absolute SPWD decrease, see Fig. S3). But more striking is the clear relationship between the magnitude of the curvature (and polarity) and the magnitude of the residual paleoaccumulation (Fig.6). The areas of high accumulation in Fig.3 are outlined in black. They correspond to areas of high positive detrended paleoaccumulation, $>$ 1.2 mm-we yr^{-1}, and are well correlated with areas of strongly positive curvature values ($>$ 2 x 10^{-7} m^{-1}). This is evident in the LDCM area. Areas of high negative detrended accumulation, $<$ -1.6 mm-we yr^{-1}, are also well correlated with areas of strongly negative curvature. This is best seen east of the CR. The correlation holds particularly well for the youngest layer (0 - 10 ka) over the entire region. We plot detrended paleoaccumulation for layers older than 10 ka, and observe that this relationship holds over the LDCM, with a slightly increasingly offset with increased ages (see S4).

4 Discussion

The 1D assumption to calculate paleoaccumulation rates is clearly the largest source of uncertainty in our reconstructions. In the 1D pseudo-steady ice flow model described in the companion paper

(Parrenin et al., 2017), the goal is to constrain the age of the deep ice. For that work, trade-offs in the strain thinning (i.e. p and G_0) and accumulation rates do not matter, as their combined effects dictate the age of the ice. However, to calculate the layer-by-layer paleoaccumulation rates, we have to assume that τ (Eq.4) is fitted perfectly, which breaks down as horizontal advection increases. We reckon that for the first layer whose average depth is ~150 m, that is ~5% of the total depth, the error in the thinning is small enough to not pollute significantly our accumulation results (total thinning is always above 0.9). For the other layers, it is difficult to imagine an error in the thinning function that would produce, by chance, a similar accumulation pattern to that of the first layer. In addition, by setting a limit on the maximum horizontal advection allowed for each age interval, the described accumulation patterns and variations are reasonably unaffected by the 1D assumption. The threshold of 5 km is chosen such that horizontal advection is negligible compared to the scale of the observed accumulation rate variability. The small-scale areas of high accumulation are at least 20 km wide in the region, therefore the 5 km threshold on horizontal movement does not affect our conclusions. We are only able to reconstruct paleoaccumulation rates back through 73 ka, therefore a 3D model is required to look at paleoaccumulation rates further back in time.

Furthermore, the model assumes a constant ice thickness through time. Even though small variations in the ice thickness through time will affect the absolute value of the reconstructed accumulation rates, the assumption of constant ice thickness is fair for the center of the EAIS where modeled ice thickness variations have been reported below 200 m (Bentley, 1999; Ritz et al., 2001; Parrenin et al., 2007) (representing a 5% error on the ice thickness), and little is known of the spatial distribution of these ice thickness variations in the center of the ice sheet. A 5% error on the ice thickness will produce a 5% error on the thinning function τ (Parrenin et al., 2007) and therefore a 5% error on the accumulation rates calculated. This error can be ignored for two reasons. First, it is small compared to the accumulation variations that we observe (larger than 10%). And second, it only affects the absolute value of the accumulation rates reconstructed but not the relative differences in accumulation rates from one location to the next in the Dome C region. Since we focus exclusively on changes in gradients and patterns in accumulation rates, this additional source of error doesn't affect our conclusions. Despite this error, we observe a clear reduction in the magnitude of the accumulation rates as we go back in time and enter the last glacial maximum, as expected and measured in ice cores (Bazin et al., 2013; Veres et al., 2013; Parrenin et al., 2017).

The observed patterns of paleoaccumulation agree well with previous studies of surface snow accumulation variability in the Dome C region. Considering first the large-scale patterns in the accumulation reconstructions, we observe a consistent large-scale gradient (large-scale here refers to 100s of kilometers) for each age interval, with accumulation values decreasing from the north side of Dome C to the south side. Scarchilli et al. (2011) suggest moisture provenance from the Indian Ocean sector is the most consistent with the clear north south gradient in precipitation observed as we near Dome C. The fact that our paleoaccumulation reconstructions reproduce the present-day large-scale surface accumulation gradient and that this remains true back to 73 ka suggests persistence of the source of moisture for this part of the East Antarctic plateau through the last glacial and deglaciation. Transects A-A' and B-B' in Fig.2 clearly show the north south orientation of the accumulation gradient. This large-scale accumulation gradient is also clearly seen in the ECMWF ERA40 data for the region (Fig.5), as well as in other large-scale accumulation models of the region (e.g. Genthon et al., 2016) or Regional Climate Model (MAR) (Gallée et al., 2013, 2015). GPR data collected during traverses across Dome C and along the divide also show a strong north-south gradient in accumulation (Urbini et al., 2008; Verfaillie et al., 2012, Emmanuel Le Meur, pers. comm.). We note a good agreement between our accumulation values and trends along A-A' going from Dome C along the ice divide towards Vostok (top panel of Fig.2) and the GPR transect measured by Verfaillie et al. (2012) on the other side of the Dome C divide. A SPRI airborne transect collected over Dome C shows a strong accumulation gradient of 10s of mm yr^{-1} over a spatial scale of 100s of km (Siegert, 2003). Urbini et al. (2008) show a small component of counter-clockwise rotation of the accumulation pattern in historical times centered on Dome C, but the general north south gradient difference in accumulation across the dome remains. Measurements made in other areas of the ice sheet, e.g. across Talos Dome (Frezzotti et al., 2007), point to similar patterns: accumulation is highest near the moisture source and decreases with distance from the coast. Fujita et al. (2011) point to the same patterns of reduced accumulation inland across Dronning Maud Land.

Considering the small-scale (10s of kilometers or a few ice thicknesses) patterns of accumulation shown earlier, we described several regions of locally increased accumulation. The co-location of the areas of higher accumulation with areas where surface slope is reduced, as seen from the surface contours or the markedly reduced SPWD values with respect to the surroundings (Fig. S3), fits well with the model put forward by Frezzotti et al. (2007). Frezzotti et al. (2007) show that accumulation increases when SPWD decreases over Talos Dome and attribute the correlation between the absolute magnitude of SPWD and accumulation rates to katabatic wind-driven ablation. Note that the prevailing wind direction over the area is more or less along the long axis of Dome C flowing from higher up the ice divide towards Dome C (see Fig.6, Frezzotti et al., 2005; Urbini et al., 2008).

The spatial correlation we obtain between the detrended paleoaccumulations and the CPWD can be explained by the same mechanisms as for SPWD, since SPWD and CPWD are directly related. Layer 0 - 10 ka shows high detrended paleoaccumulation values where the surface curvature is strongly positive (i.e. surface trough), and low values where the surface curvature is strongly negative (i.e. surface bump). This is true for both the LCDM and CR regions. The proximity of the isochrone-bounded layer to the surface influences how well the correlation holds, particularly visible in the CR region which is furthest from the divide. For any deeper layer (Fig.S4), this relationship is slightly offset in space; a likely cause is the increased amount of horizontal advection with depth, up to the set maximum of 5 km .

Even though the absolute magnitudes of slope and curvature changes we observe are relatively small (on the order of 10^{-3} and 10^{-7} m^{-1}, respectively), other studies have shown that even very small slope changes can have a strong influence on wind-borne redistribution of snow (Grima et al., 2014; King et al., 2004; Whillans, 1975). However a single mechanism has yet to be described that would explain the relationship between CPWD (and therefore SPWD) and small-scale accumulation variations. Grima et al. (2014) observe strong surface density variations linked to surface slope breaks, however some increases in accumulation occur over steeper surface slopes, which is surprising when steep slopes are usually associated with reduced accumulation (Hamilton, 2004; Frezzotti et al., 2004). King et al. (2004) show that local slope changes of 0.01 can create up to 30% variations in accumulation, and invoke a highly non-linear relationship between wind speed and snow transport to explain the type of accumulation variability they observe. Whillans (1975) also shows that slope changes as small as 0.001 over a distance of 3 km can affect snow deposition, and argues for a relationship between slope, wind strength and mass drift drift transport.

The extreme pattern of high and low accumulation parallel to the CST and east of the CR seems to be the ideal example of how surface topography variations affect accumulation rates. The ice flowing radially away from Dome C has to flow over the CST and the prominent bedrock CR. CPWD shows strongly negative values over the subglacial CR; it creates a surface which is concave down perpendicular to the wind direction. We can imagine a scenario in which snow is strongly plucked away on this steepest surface slope, but further down-wind, as slope reduces and reaches contrastingly strongly positive CPWD, the snow can then be redeposited directly down-wind as suggested in Frezzotti et al. (2004).

We attempted a series of low order (linear and quadratic) fits between CPWD and our detrended paleoaccumulations but none explain all the variability. The data is suggestive of threshold behaviors between low and high CPWD magnitudes. ECMWF wind speed magnitudes over the LDCM and CR areas (Simmons et al., 2007) are below the 5 m s^{-1} threshold for dune processes to be active in the region, and the radar data used do not show any buried dune structures. The accumulation patterns observed are more suggestive of the preferential infill of surface troughs by winds. These troughs might not fill-up easily because of the very low surface precipitation rates in the region (Genthon et al., 2016; Urbini et al., 2008) combined with the presence of areas of subglacial melting in the region (Young et al., 2017), creating additional draw-down of the surface.

We noted in the results that the small-scale accumulation variations were co-located with bedrock relief variations (see Fig. S1). Frezzotti et al. (2007) explain that bedrock topography can be the underlying influence on the variability of snow accumulation at scales of 1-20 km, corresponding to the lengthscales of the accumulation variations we calculate here. Bedrock topography will have a stronger influence on the overlying ice in the presence of subglacial lubrication (Rémy et al., 2003). Rémy et al. (2003) show that for the Dome C region, the most positive surface curvatures are directly linked to the largest ice thicknesses and the presence of subglacial lakes. It is interesting to note that areas of higher detrended paleoaccumulation correlated to high positive CPWD outlined in Fig.3 are above deep bedrock valleys dotted with many observed subglacial lakes (Young et al., 2017).

Although we cannot yet explain the mechanisms causing the small-scale paleoaccumulation variability we observe in the Dome C region, which is beyond the scope of this manuscript, our observations have important ramifications for better understanding the region's stability through time. In the future, we hope to improve our paleoaccumulation rate reconstructions, and in particular go back further into the last glacial cycle with a full 3D model. Further GPR data was recently collected over the LDCM, and strain nets and various other instruments have been deployed. These new measurements will add to the existing data set and provide important constraints if we hope to develop 3D inversions.

5 Conclusions

We reconstructed accumulation rates for the last 73 kyrs. Looking at both large- and small-scale accumulation gradients, we show that these have not changed significantly since the last glacial. Large-scale accumulation gradients will remain constant if moisture-bearing air mass trajectory interactions with surface topography do not vary. Small-scale accumulation variations are strongly controlled by SPWD and CPWD and therefore, if the pattern of high and low accumulations remains fixed over a long period of time, this requires consistent interactions between local surface slopes and prevailing winds over the last 73 kyrs, independent of whether the control comes from the bedrock topography and/or potential basal melting. This points to a spatially stationary and persistent accumulation pattern in the Dome C region over the last glacial, an important constraint for modeling efforts in the area, both for dating existing ice cores as well as for the prospecting of a 1.5 million-year-old ice core site.

6 Data accessibility

The radar isochrones used in this manuscript will be made publicly available in 2018 as a separate publication. Code for the model is available publicly under https://github.com/parrenin/IsoInv.

7 Author contributions

M.G.P. Cavitte interpreted and analysed the radar isochrones, F. Parrenin developed the model and ran experiments with M.G.P. Cavitte with C. Ritz input, D.A. Young, J.L Roberts and D.D. Blankenship were involved in survey design and data acquisition, B. Van Liefferinge and M. Frezzotti provided data and discussion material. M.G.P. Cavitte prepared the manuscript with contributions from all co-authors. The authors declare that they have no conflicts of interest.

Acknowledgements. This publication was generated in the frame of Beyond EPICA-Oldest Ice (BE-OI). The project has received funding from the European Union's Horizon 2020 research and innovation programme under grant agreement No. 730258 (BE-OI CSA). It has received funding from the Swiss State Secretariate for Education, Research and Innovation (SERI) under contract number 16.0144. It is furthermore supported by national partners and funding agencies in Belgium, Denmark, France, Germany, Italy, Norway, Sweden, Switzerland, The Netherlands and the United Kingdom. Logistic support is mainly provided by AWI, BAS, ENEA and IPEV. The opinions expressed and arguments employed herein do not necessarily reflect the official views of the European Union funding agency, the Swiss Government or other national funding bodies. This research was made possible by the joint French–Italian Concordia Program, which established and runs the permanent station Concordia at Dome C. This work was supported by NSF grants ANT-0733025, ARC-0941678, and PLR-1443690, NASA grants NNX08AN68G, NNX09AR52G, and NNX11AD33G (Operation Ice Bridge) to Texas, the Jackson School of Geosciences, the Gale White UTIG Fellowship, the G. Unger Vetlesen Foundation, NERC grant NE/D003733/1, the Global Innovation Initiative award from the British Council, the Australian Government's Cooperative Research Centre's Programme through the Antarctic Climate and Ecosystems Cooperative Research Centre (ACE CRC). Operational support was provided by the U. S. Antarctic Program and by the Institut Polaire Français Paul Emile Victor (IPEV) and the Italian Antarctic Program (PNRA and ENEA) and the Australian Antarctic Division provided funding and logistical support (AAS 3103, 4077, 4346). We acknowledge the support of Kenn Borek Airlines. Additional support was provided by the French ANR Dome A project (ANR-07-BLAN-0125), the CNRS/INSU/LEFE fundings "IceChrono" and "CO2Role" and the Grenoble-Alpes University AGIR funding "Oldest Ice". Special thanks to Dr. Olivier Passalacqua for fruitful discussions. This is BE-OI publication number ####. This is UTIG contribution 3116.

References

Albani, S., Delmonte, B., Maggi, V., Baroni, C., Petit, J., Stenni, B., Mazzola, C., and Frezzotti, M.: Interpreting last glacial to Holocene dust changes at Talos Dome (East Antarctica): implications for atmospheric variations from regional to hemispheric scales, Climate of the Past, 8, 741–750, 2012.

Arthern, R. J., Winebrenner, D. P., and Vaughan, D. G.: Antarctic snow accumulation mapped using polarization of 4.3-cm wavelength microwave emission, Journal of Geophysical Research: Atmospheres, 111, 2006.

Bamber, J., Gomez-Dans, J., and Griggs, J.: A new 1 km digital elevation model of the Antarctic derived from combined satellite radar and laser data–Part 1: Data and methods, The Cryosphere, 3, 101–111, doi:10.5194/tc-3-101-2009, 2009.

Bazin, L., Landais, A., Lemieux-Dudon, B., Toyé Mahamadou Kele, H., Veres, D., Parrenin, F., Martinerie, P., Ritz, C., Capron, E., Lipenkov, V., et al.: An optimized multi-proxy, multi-site Antarctic ice and gas orbital chronology (AICC2012): 120-800 ka, Climate of the Past, 9, 1715–1731, doi:10.5194/cp-9-1715-2013, 2013.

Bentley, M. J.: Volume of Antarctic ice at the Last Glacial Maximum, and its impact on global sea level change, Quaternary Science Reviews, 18, 1569–1595, 1999.

Bingham, R. G. and Siegert, M. J.: Quantifying subglacial bed roughness in Antarctica: implications for ice-sheet dynamics and history, Quaternary Science Reviews, 28, 223–236, 2009.

Black, H. and Budd, W.: Accumulation in the region of Wilkes, Wilkes Land, Antarctica, Journal of Glaciology, 5, 3–15, 1964.

Bromwich, D. H., Guo, Z., Bai, L., and Chen, Q.-s.: Modeled Antarctic precipitation. Part I: Spatial and temporal variability, Journal of Climate, 17, 427–447, 2004.

Budd, W.: An analysis of the relation between the surface and bedrock profiles of ice caps, Journal of Glaciology, 10, 197–209, 1971.

Cavitte, M. G., Blankenship, D. D., Young, D. A., Schroeder, D. M., Parrenin, F., Lemeur, E., Macgregor, J. A., and Siegert, M. J.: Deep radiostratigraphy of the East Antarctic plateau: connecting the Dome C and Vostok ice core sites, Journal of Glaciology, 62, 323–334, 2016.

Das, I., Bell, R. E., Scambos, T. A., Wolovick, M., Creyts, T. T., Studinger, M., Frearson, N., Nicolas, J. P., Lenaerts, J. T., and van den Broeke, M. R.: Influence of persistent wind scour on the surface mass balance of Antarctica, Nature Geoscience, 6, 367–371, doi:10.1038/ngeo1766, 2013.

Delmonte, B., Andersson, P., Schöberg, H., Hansson, M., Petit, J., Delmas, R., Gaiero, D., Maggi, V., and Frezzotti, M.: Geographic provenance of aeolian dust in East Antarctica during Pleistocene glaciations: preliminary results from Talos Dome and comparison with East Antarctic and new Andean ice core data, Quaternary Science Reviews, 29, 256–264, 2010.

Drewry, D., Meldrum, D., and Jankowski, E.: Radio echo and magnetic sounding of the Antarctic ice sheet, 1978–79, Polar Record, 20, 43–51, 1980.

Fischer, H., Severinghaus, J., Brook, E., Wolff, E., Albert, M., Alemany, O., Arthern, R., Bentley, C., Blankenship, D., Chappellaz, J., et al.: Where to find 1.5 million year old ice for the IPICS “Oldest Ice” ice core, Climate of the Past, 9, 2489–2505, 2013.

Fretwell, P., Pritchard, H. D., Vaughan, D. G., Bamber, J., Barrand, N., Bell, R., Bianchi, C., Bingham, R., Blankenship, D., Casassa, G., et al.: Bedmap2: improved ice bed, surface and thickness datasets for Antarctica, The Cryosphere, 7, 2013.

Frezzotti, M., Gandolfi, S., La Marca, F., and Urbini, S.: Snow dunes and glazed surfaces in Antarctica: new field and remote-sensing data, Annals of Glaciology, 34, 81–88, 2002a.

Frezzotti, M., Gandolfi, S., and Urbini, S.: Snow megadunes in Antarctica: sedimentary structure and genesis, Journal of Geophysical Research: Atmospheres, 107, 2002b.

Frezzotti, M., Pourchet, M., Flora, O., Gandolfi, S., Gay, M., Urbini, S., Vincent, C., Becagli, S., Gragnani, R., Proposito, M., et al.: New estimations of precipitation and surface sublimation in East Antarctica from snow accumulation measurements, Climate Dynamics, 23, 803–813, 2004.

Frezzotti, M., Pourchet, M., Flora, O., Gandolfi, S., Gay, M., Urbini, S., Vincent, C., Becagli, S., Gragnani, R., Proposito, M., et al.: Spatial and temporal variability of snow accumulation in East Antarctica from traverse data, Journal of Glaciology, 51, 113–124, 2005.

Frezzotti, M., Urbini, S., Proposito, M., Scarchilli, C., and Gandolfi, S.: Spatial and temporal variability of surface mass balance near Talos Dome, East Antarctica, Journal of Geophysical Research: Earth Surface, 112, 2007.

Fujita, S., Holmlund, P., Andersson, I., Brown, I., Enomoto, H., Fujii, Y., Fujita, K., Fukui, K., Furukawa, T., Hansson, M., et al.: Spatial and temporal variability of snow accumulation rate on the East Antarctic ice divide between Dome Fuji and EPICA DML, The Cryosphere, 5, 1057–1081, 2011.

Gallée, H., Trouvilliez, A., Agosta, C., Genthon, C., Favier, V., and Naaim-Bouvet, F.: Transport of snow by the wind: a comparison between Observations in Adélie Land, Antarctica, and Simulations made with the Regional Climate Model MAR, Boundary-layer meteorology, pp. 1–15, 2013.

Gallée, H., Preunkert, S., Argentini, S., Frey, M., Genthon, C., Jourdain, B., Pietroni, I., Casasanta, G., Barral, H., Vignon, E., et al.: Characterization of the boundary layer at Dome C (East Antarctica) during the OPALE summer campaign, Atmospheric Chemistry and Physics, 15, 6225–6236, 2015.

Genthon, C., Six, D., Scarchilli, C., Ciardini, V., and Frezzotti, M.: Meteorological and snow accumulation gradients across Dome C, East Antarctic plateau, International Journal of Climatology, 36, 455–466, doi:10.1002/joc.4362, http://dx.doi.org/10.1002/joc.4362, 2016.

Grima, C., Blankenship, D. D., Young, D. A., and Schroeder, D. M.: Surface slope control on firn density at Thwaites Glacier, West Antarctica: Results from airborne radar sounding, Geophysical Research Letters, 41, 6787–6794, 2014.

Gudmandsen, P.: Electromagnetic probing of ice, in: Electromagnetic probing in geophysics, vol. 1, p. 321, 1971.

Hamilton, G. S.: Topographic control of regional accumulation rate variability at South Pole and implications for ice-core interpretation, Annals of Glaciology, 39, 214–218, 2004.

Kållberg, P., Simmons, A., Uppala, S., and Fuentes, M.: The ERA-40 archive. [Revised October 2007], Shinfield Park, Reading, 2004.

King, J., Anderson, P., Vaughan, D., Mann, G., Mobbs, S., and Vosper, S.: Wind-borne redistribution of snow across an Antarctic ice rise, Journal of Geophysical Research: Atmospheres, 109, 2004.

Koutnik, M. R., Fudge, T., Conway, H., Waddington, E. D., Neumann, T. A., Cuffey, K. M., Buizert, C., and Taylor, K. C.: Holocene accumulation and ice flow near the West Antarctic Ice Sheet Divide ice core site, Journal of Geophysical Research: Earth Surface, 121, 907–924, 2016.

Leysinger Vieli, G. J., Hindmarsh, R. C., Siegert, M. J., and Bo, S.: Time-dependence of the spatial pattern of accumulation rate in East Antarctica deduced from isochronic radar layers using a 3-D numerical ice flow model, Journal of Geophysical Research: Earth Surface (2003–2012), 116, doi:10.1029/2010JF001785, 2011.

MacGregor, J. A., Matsuoka, K., Waddington, E. D., Winebrenner, D. P., and Pattyn, F.: Spatial variation of englacial radar attenuation: modeling approach and application to the Vostok flowline, Journal of Geophysical Research: Earth Surface (2003–2012), 117, 2012.

MacGregor, J. A., Fahnestock, M. A., Catania, G. A., Paden, J. D., Gogineni, S., Young, S. K., Rybarski, S. C., Mabrey, A. N., Wagman, B. M., and Morlighem, M.: Radiostratigraphy and age structure of the Greenland Ice Sheet, Journal of Geophysical Research: Earth Surface, 120, 212–241, doi:10.1002/2014JF003215, 2015.

Martin, C., Hindmarsh, R. C., and Navarro, F. J.: On the effects of divide migration, along-ridge flow, and basal sliding on isochrones near an ice divide, Journal of Geophysical Research: Earth Surface, 114, 2009.

Medley, B., Joughin, I., Das, S. B., Steig, E. J., Conway, H., Gogineni, S., Criscitiello, A. S., McConnell, J. R., Smith, B., Broeke, M., et al.: Airborne-radar and ice-core observations of annual snow accumulation over Thwaites Glacier, West Antarctica confirm the spatiotemporal variability of global and regional atmospheric models, Geophysical Research Letters, 40, 3649–3654, 2013.

Millar, D.: Radio-echo layering in polar ice sheets and past volcanic activity, Nature, 292, 441–443, doi:10.1038/292441a0, 1981.

Morse, D., Waddington, E., and Steig, E.: Ice age storm trajectories inferred from radar stratigraphy at Taylor Dome, Antarctica, Geophysical Research Letters, 25, 3383–3386, 1998.

Nereson, N. A. and Waddington, E. D.: Isochrones and isotherms beneath migrating ice divides, Journal of Glaciology, 48, 95–108, 2002.

Neumann, T., Conway, H., Price, S., Waddington, E., Catania, G., and Morse, D.: Holocene accumulation and ice sheet dynamics in central West Antarctica, Journal of Geophysical Research: Earth Surface, 113, 2008.

Palerme, C., Kay, J. E., Genthon, C., L'Ecuyer, T., Wood, N. B., and Claud, C.: How much snow falls on the Antarctic ice sheet?, The Cryosphere, 8, 1577–1587, doi:10.5194/tc-8-1577-2014, http://www.the-cryosphere.net/8/1577/2014/, 2014.

Parrenin, F. and Hindmarsh, R.: Influence of a non-uniform velocity field on isochrone geometry along a steady flowline of an ice sheet, Journal of Glaciology, 53, 612–622, 2007.

Parrenin, F., Hindmarsh, R., and Rémy, F.: Analytical solutions for the effect of topography, accumulation rate and lateral flow divergence on isochrone layer geometry, Journal of Glaciology, 52, 191–202, 2006.

Parrenin, F., Dreyfus, G., Durand, G., Fujita, S., Gagliardini, O., Gillet, F., Jouzel, J., Kawamura, K., Lhomme, N., Masson-Delmotte, V., et al.: 1-D-ice flow modelling at EPICA Dome C and Dome Fuji, East Antarctica, Climate of the Past, 3, 243–259, 2007.

Parrenin, F., Cavitte, M. G. P., Blankenship, D. D., Chappellaz, J., Fischer, H., Gagliardini, O., Masson-Delmotte, V., Passalacqua, O., Ritz, C., Roberts, J., Siegert, M. J., and Young, D. A.: Is there 1.5-million-year-old ice near Dome C, Antarctica?, The Cryosphere, 11, 2427–2437, doi:10.5194/tc-11-2427-2017, https://www.the-cryosphere.net/11/2427/2017/, 2017.

Rémy, F., Testut, L., Legrésy, B., Forieri, A., Bianchi, C., and Tabacco, I. E.: Lakes and subglacial hydrological networks around Dome C, East Antarctica, Annals of Glaciology, 37, 252–256, 2003.

Ritz, C., Rommelaere, V., and Dumas, C.: Modeling the evolution of Antarctic ice sheet over the last 420,000 years: Implications for altitude changes in the Vostok region, Journal of Geophysical Research: Atmospheres, 106, 31 943–31 964, 2001.

Scarchilli, C., Frezzotti, M., and Ruti, P. M.: Snow precipitation at four ice core sites in East Antarctica: provenance, seasonality and blocking factors, Climate dynamics, 37, 2107–2125, 2011.

Siegert, M. J.: On the origin, nature and uses of Antarctic ice-sheet radio-echo layering, Progress in physical geography, 23, 159–179, doi:10.1177/030913339902300201, 1999.

Siegert, M. J.: Glacial–interglacial variations in central East Antarctic ice accumulation rates, Quaternary Science Reviews, 22, 741–750, 2003.

Simmons, A., Uppala, S., Dee, D., and Kobayashi, S.: ERA-Interim: New ECMWF reanalysis products from 1989 onwards, ECMWF newsletter, 110, 25–35, 2007.

Stenni, B., Scarchilli, C., Masson-Delmotte, V., Schlosser, E., Ciardini, V., Dreossi, G., Grigioni, P., Bonazza, M., Cagnati, A., Karlicek, D., et al.: Three-year monitoring of stable isotopes of precipitation at Concordia Station, East Antarctica, The Cryosphere, 10, 2415, 2016.

Urbini, S., Frezzotti, M., Gandolfi, S., Vincent, C., Scarchilli, C., Vittuari, L., and Fily, M.: Historical behaviour of Dome C and Talos Dome (East Antarctica) as investigated by snow accumulation and ice velocity measurements, global and planetary change, 60, 576–588, 2008.

Van de Berg, W., Van den Broeke, M., Reijmer, C., and Van Meijgaard, E.: Reassessment of the Antarctic surface mass balance using calibrated output of a regional atmospheric climate model, Journal of Geophysical Research: Atmospheres, 111, 2006.

Van Liefferinge, B. and Pattyn, F.: Using ice-flow models to evaluate potential sites of million year-old ice in Antarctica, Climate of the Past, 9, 2335, 2013.

Van Wessem, J., Reijmer, C., Morlighem, M., Mouginot, J., Rignot, E., Medley, B., Joughin, I., Wouters, B., Depoorter, M., Bamber, J., Lenaerts, J., De Van Berg, W., Van Den Broeke, M., and Van Meijgaard, E.: Improved representation of East Antarctic surface mass balance in a regional atmospheric climate model, Journal of Glaciology, 60, 761–770, doi:doi:10.3189/2014JoG14J051, 2014.

Veres, D., Bazin, L., Landais, A., Toyé Mahamadou Kele, H., Lemieux-Dudon, B., Parrenin, F., Martinerie, P., Blayo, E., Blunier, T., Capron, E., et al.: The Antarctic ice core chronology (AICC2012): an optimized multi-parameter and multi-site dating approach for the last 120 thousand years, Climate of the Past, 9, 1733–1748, doi:10.5194/cp-9-1733-2013, 2013.

Verfaillie, D., Fily, M., Le Meur, E., Magand, O., Jourdain, B., Arnaud, L., and Favier, V.: Snow accumulation variability derived from radar and firn core data along a 600 km transect in Adelie Land, East Antarctic plateau, The Cryosphere, 6, 1345–1358, 2012.

Waddington, E. D., Neumann, T. A., Koutnik, M. R., Marshall, H.-P., and Morse, D. L.: Inference of accumulation-rate patterns from deep layers in glaciers and ice sheets, Journal of Glaciology, 53, 694–712, 2007.

Whillans, I. M.: Effect of inversion winds on topographic detail and mass balance on inland ice sheets, Journal of Glaciology, 14, 85–90, 1975.

Young, D. A., Roberts, J. L., Ritz, C., Frezzotti, M., Quartini, E., Cavitte, M. G. P., Tozer, C. R., Steinhage, D., Urbini, S., Corr, H. F. J., van Ommen, T., and Blankenship, D. D.: High-resolution boundary conditions of an old ice target near Dome C, Antarctica, The Cryosphere, 11, 1897–1911, doi:10.5194/tc-11-1897-2017, https://www.the-cryosphere.net/11/1897/2017/, 2017.

Table 1: Radar isochrones and their uncertainties at the Dome C ice core site.

Isochrone	**Depth (m)**	**Depth uncertainty (±m)**	**Age (ka)**	**Age uncertainty (±ka)**
1	307.61	1.82	9.97	0.26
2	699.60	2.29	38.11	0.61
3	798.60	2.31	46.41	0.80
4	1076.10	3.11	73.37	2.07

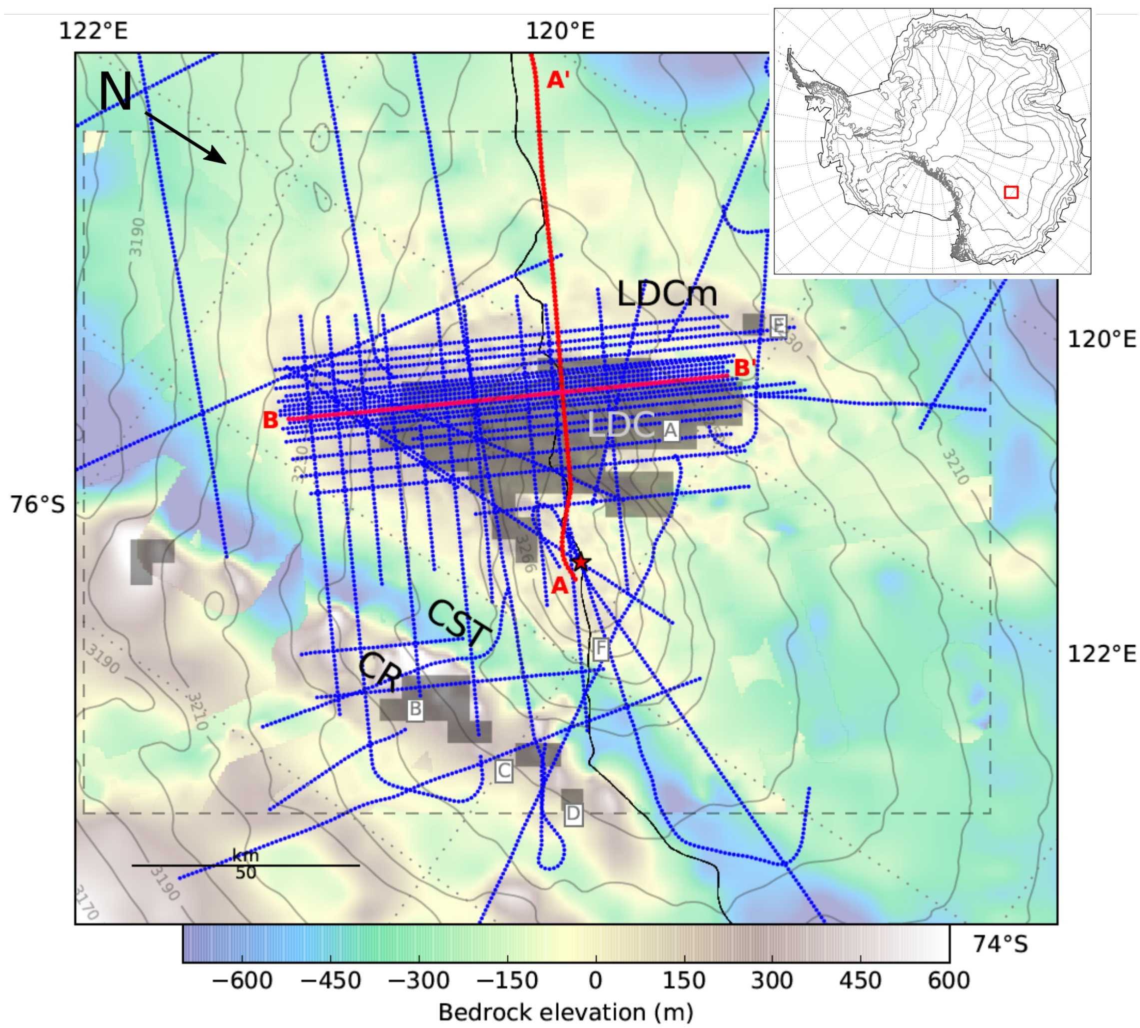

Figure 1: Map of Dome C and the surrounding region. A red square locates the study area on the inset. The radar lines used in the accumulation reconstructions are displayed as blue lines. Highlighted in red are the two radar lines shown in Fig.2. Dark gray blocks labeled A-E are the Van Liefferinge and Pattyn (2013) Candidate regions. F labels a 1.5 million-year-old ice new Candidate site (see companion paper). The background is bedrock elevation in meters above sea level and combines Bedmap2 bed elevations (Fretwell et al., 2013) as well as a recompilation based on the OIA radar bed elevations (Young et al., 2017) delimited by a dashed rectangle (elevation differences are particularly visible along the CR). Gray contours are Bamber et al. (2009) surface elevations, a black line locates the ice divide. A red star locates the EPICA Dome C ice core. LDC locates the gentle secondary surface dome, LDCM locates the Little Dome C massif under the densest radar lines, CR locates the Concordia Ridge steep escarpment along the Concordia Subglacial Trench (CST).

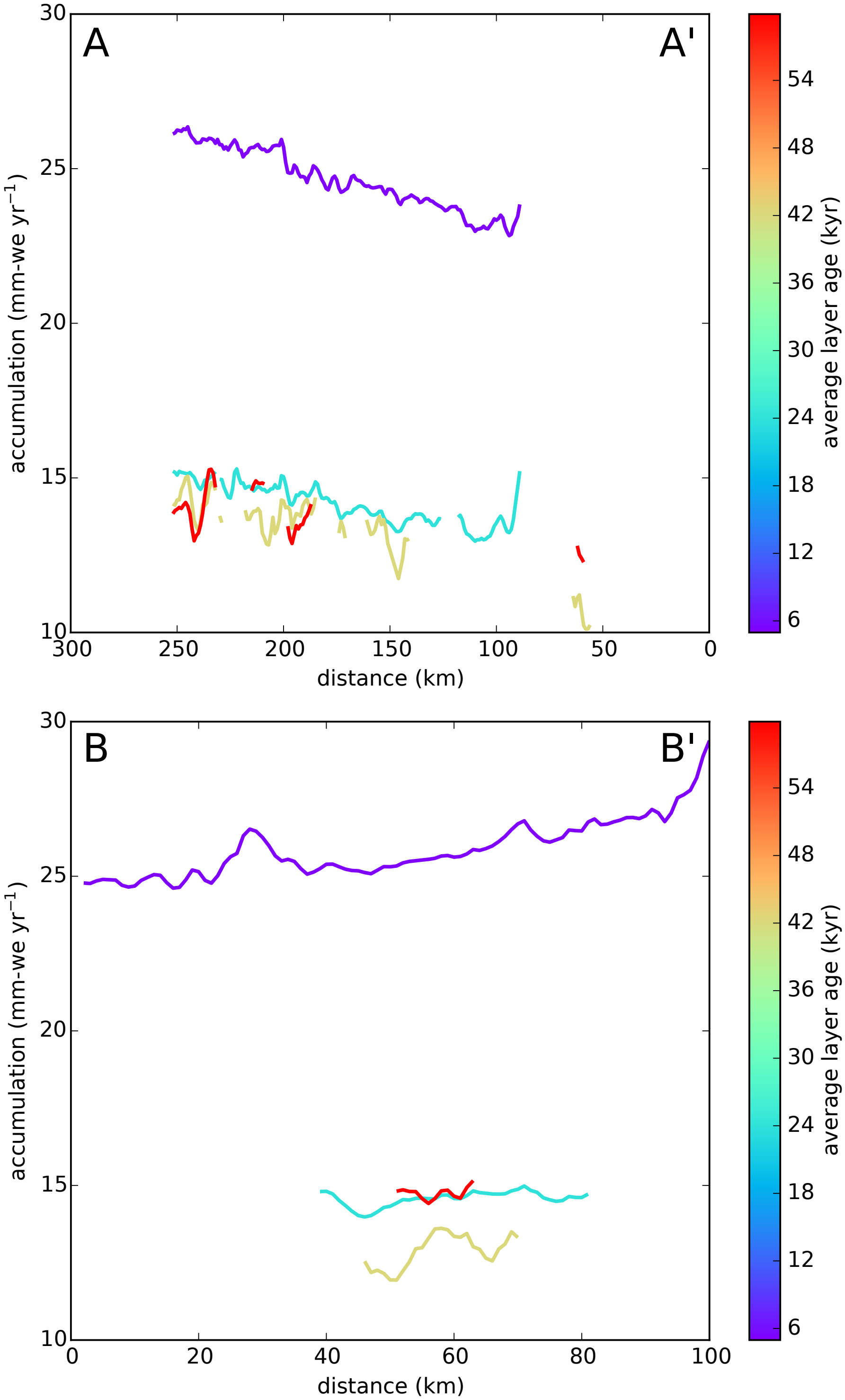

Figure 2: Paleoaccumulation rates along radar lines. Colors represent the mean of the age interval $\Delta\chi$ for each layer. Top panel shows the reconstructed paleoaccumulation rate $a_{o,\Delta\chi}$ along the A-A' radar line. Bottom panel is along the B-B' radar line. Both radar lines are highlighted on Fig.1, distance represents kilometers along each radar line. Results are filtered to remove regions of excess horizontal strain. A-A', along the ice divide, displays a strong and consistent accumulation gradient. B-B', perpendicular to the ice divide, shows no gradient except a weaker one for the interglacial 10 ka isochrone on its southern edge.

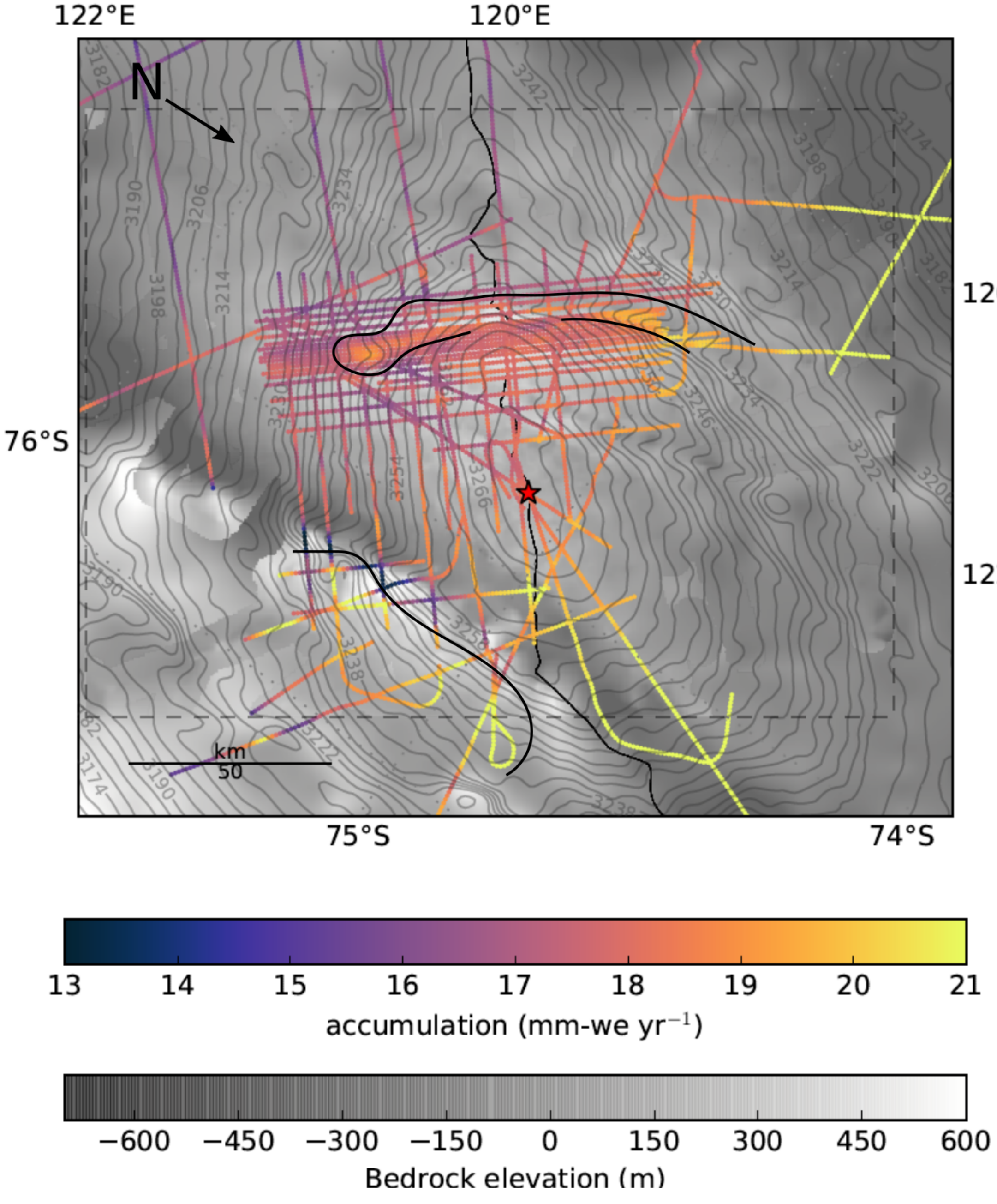

Figure 3: Time-averaged accumulation rates $\bar{a}$ along the radar lines over the Dome C region. Accumulation rates are given in mm of water equivalent per year. There is a clear large-scale N-S accumulation gradient, with accumulation decreasing with distance from the Indian Ocean coast, the main pathway of snow precipitation. Black lines outline areas of small-scale high accumulation: they correlate to areas where surface contours (in gray) become further apart, i.e. where surface slope is reduced. Background is the same as in Fig.1.

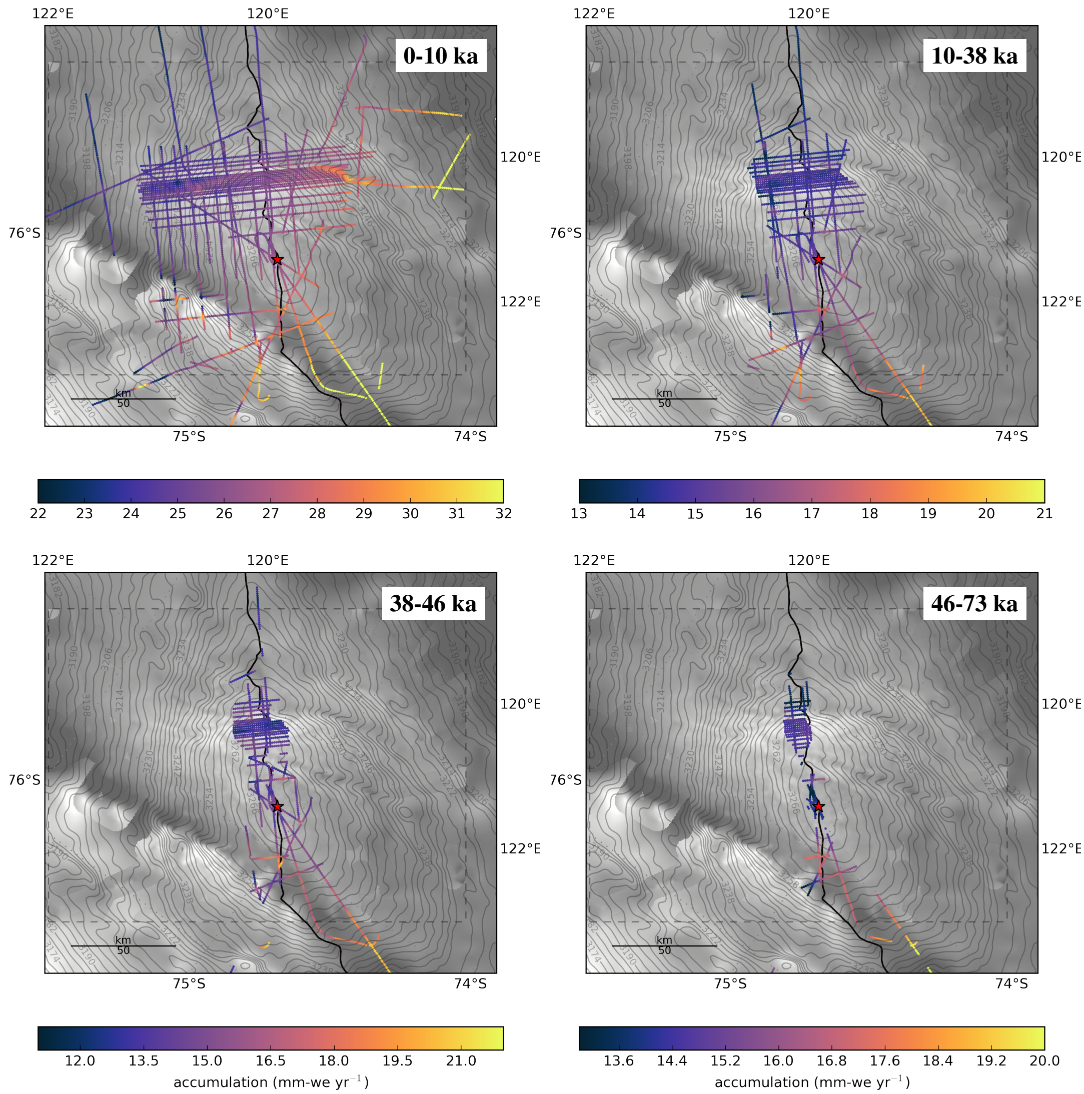

Figure 4: Paleoaccumulation reconstruction over the Dome C region since 73 ka. Panels show paleoaccumulation rates calculated for each isochrone-bounded layer, age intervals are given on each panel. Results are filtered to remove regions of excess horizontal strain. The north south accumulation rate gradient, decreasing with distance from the Indian Ocean coastal sector, remains stable for the last 73 ka. Background is the same as in Fig.1.

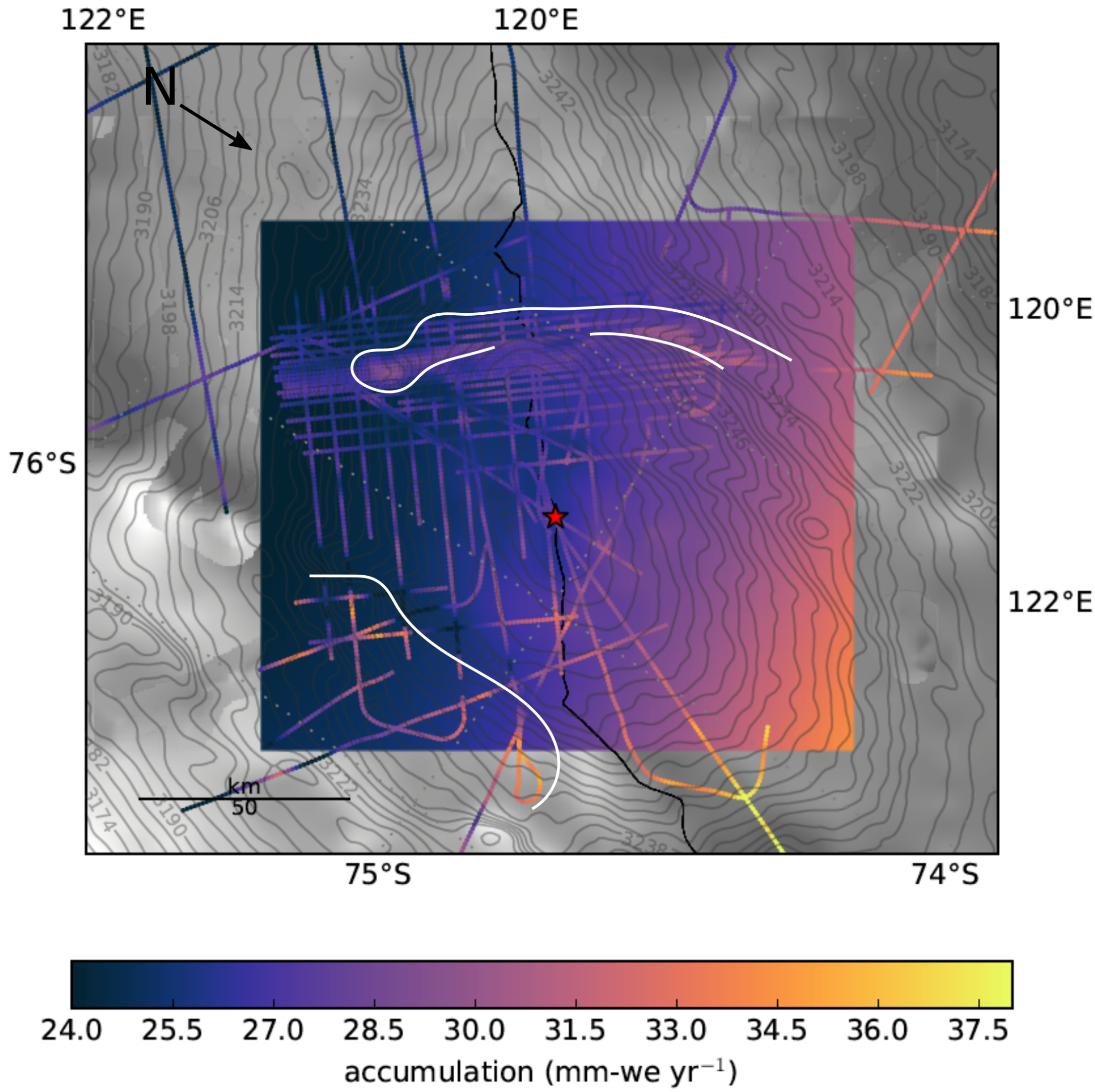

Figure 5: Holocene average accumulation rates a_{100yrs} along the radar lines superimposed on ECMWF ERA40 estimated present-day surface accumulation rates (see Sect.2.4). There is a very good agreement in the magnitude of accumulation values between the two datasets and in their north south accumulation gradient on large-scales (100s km), with accumulation decreasing with distance from the coast. White lines outline the same areas of small-scale high accumulation as in Fig.3. Background is the same as in Fig.1.

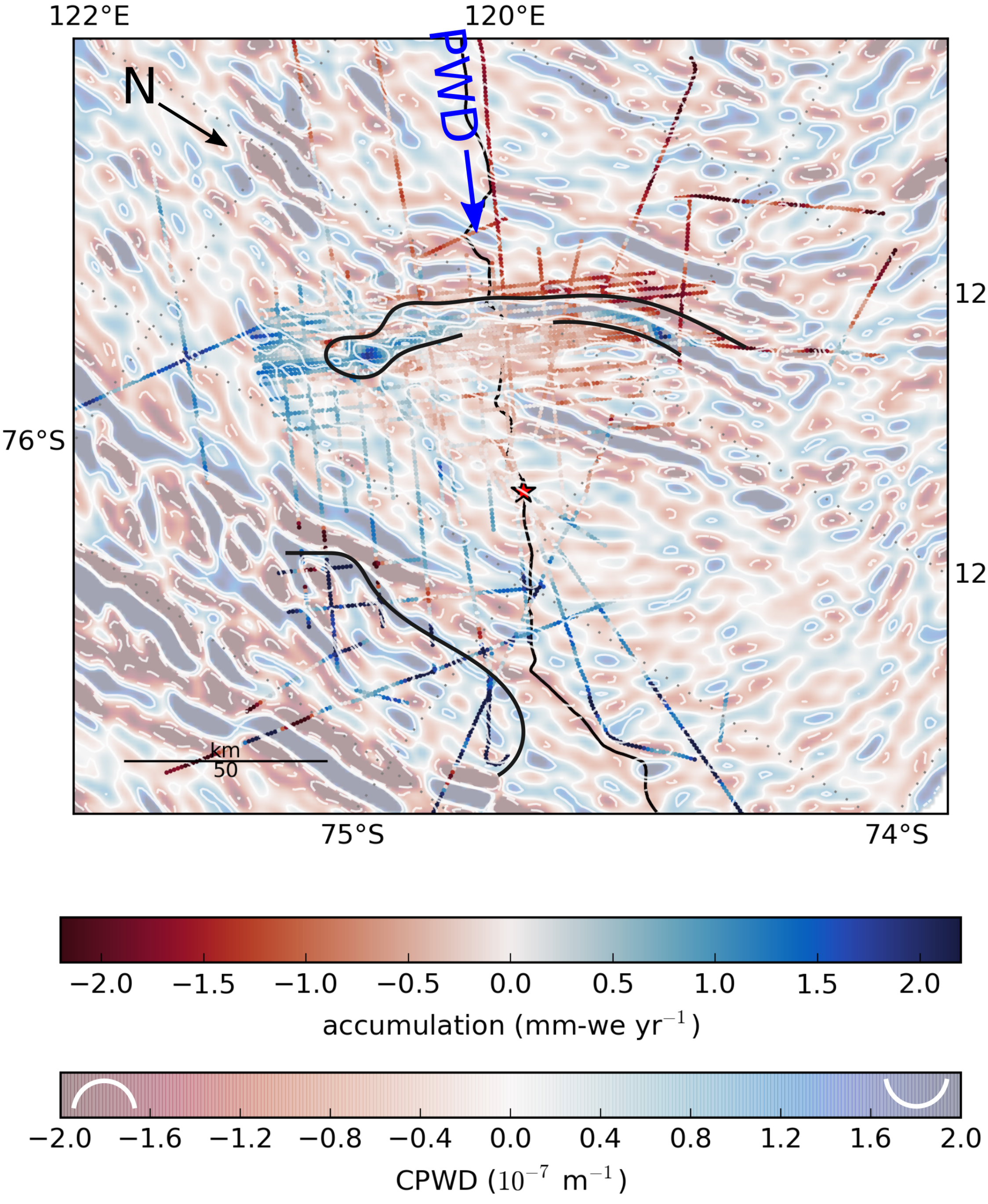

Figure 6: Residual paleoaccumulations over the region for the 0 - 10 ka age interval, overlain on surface curvature in the prevailing wind direction (CPWD, strongly positive and negative values are sketched on either end of the colorbar). Black lines outline the same areas of small-scale high accumulation as on Fig.3 and 5. Results are filtered to remove regions of excess horizontal strain. The residual paleoaccumulation highs correlate well to areas of strongly positive CPWD. A blue arrow indicates prevailing wind direction.